nature neuroscience

# Parvalbumin interneurons provide grid cell–driven recurrent inhibition in the medial entorhinal cortex

Christina Buetfering, Kevin Allen & Hannah Monyer

**Grid cells in the medial entorhinal cortex (MEC) generate metric spatial representations. Recent attractor-network models suggest an essential role for GABAergic interneurons in the emergence of the grid-cell firing pattern through recurrent inhibition dependent on grid-cell phase. To test this hypothesis, we studied identified parvalbumin-expressing (PV$^+$) interneurons that are the most likely candidate for providing this recurrent inhibition onto grid cells. Using optogenetics and tetrode recordings in mice, we found that PV$^+$ interneurons exhibited high firing rates, low spatial sparsity and no spatial periodicity. PV$^+$ interneurons inhibited all functionally defined cell types in the MEC and were in turn recruited preferentially by grid cells. To our surprise, we found that individual PV$^+$ interneurons received input from grid cells with various phases, which most likely accounts for the broadly tuned spatial firing activity of PV$^+$ interneurons. Our data argue against the notion that PV$^+$ interneurons provide phase-dependent recurrent inhibition and challenge recent attractor-network models of grid cells.**



The MEC is one of several interconnected brain regions that generate internal spatial representations critical for navigation and spatial memory[1–4]. MEC neurons exhibit distinct modes of spatial activity, the most common being that of grid cells whose periodic spatial firing coincides with the vertices of a grid of equilateral triangles[1]. The MEC also contains neurons that are modulated by the head direction of the animal[5], by the animal's distance from a geometric border[6] or by a combination of periodic spatial firing and head-direction selectivity[5]. The activity of these functionally defined neurons is regulated by local GABAergic inhibitory interneurons[7]. Approximately half of GABAergic interneurons in the MEC express parvalbumin (PV)[8,9] and form a dense axonal plexus that is a major source of inhibitory synapses onto both excitatory and inhibitory cells of layer II and III (refs. 8,10–12).

Computational MEC network models provide mechanistic explanations for grid-cell periodicity. The models include oscillatory interference[13,14], spike adaptation[15] and attractor-network models[16–18]. The latter propose that the grid-cell firing pattern results from local connectivity in the MEC network. Earlier implementations used direct excitatory connections between grid cells, such that the degree of firing-field overlap between grid cells (i.e., grid-cell phase similarity) determines connection strength[16,17]. However, direct probing for excitatory connections between MEC neurons *in vitro* revealed that layer II stellate cells, putative grid cells[19,20], are not or extremely sparsely interconnected[7,21–23]. These experimental data motivated the development of attractor-network models in which the connections between grid cells are inhibitory[18,21,22,24]. Thus, in these attractor-network models, inhibitory connectivity dependent on grid-cell phase is a prerequisite for the generation of grid-cell periodicity.

An explicit model of GABAergic interneurons has been generated, providing recurrent inhibition to grid cells[22]. In such a connectivity scheme, grid cells connect only onto GABAergic interneurons, which in turn project back only onto grid cells. Therefore grid cells impose a well-defined spatial firing pattern onto GABAergic interneurons. Depending on the precise configuration of the connections between excitatory and inhibitory cells, the model in ref. 22 predicts that GABAergic interneurons display either grid cell–like firing fields or inverted grid cell–like firing fields. Although GABAergic interneurons have not been explicitly implemented in other attractor-network models using recurrent inhibition[18,21,24], one can infer that GABAergic interneurons in these models would also inherit grid cell–like firing fields because inhibitory connections originated directly from grid cells.

The wealth of information based on modeling data is in sharp contrast with the scarcity of empirical data regarding properties and connectivity of identified MEC neurons. Here we performed tetrode recordings from functionally defined MEC neurons combined with optogenetic stimulation that allow the identification and manipulation of PV$^+$ interneurons[25]. Our results demonstrate that PV$^+$ interneurons exhibit no grid cell–like firing fields or inverted grid cell–like firing fields[22]. In the local network of the MEC, PV$^+$ interneurons provide inhibitory feedback onto most spatially selective MEC neurons and are themselves recruited preferentially by local grid cells. Notably, PV$^+$ interneurons integrate input from grid cells with various phases, which speaks against PV$^+$ interneurons being involved in mediating grid cell phase–dependent recurrent inhibition in the local MEC microcircuit.

## RESULTS

### Identification of PV$^+$ interneurons in the MEC

We selectively expressed channelrhodopsin-2 (ChR2) in PV$^+$ interneurons of the MEC in order to identify them and manipulate their activity in awake mice. We injected an adeno-associated virus expressing ChR2-mCherry upon activity of Cre recombinase into the MEC of *PV-Cre* mice[25–27] in which Cre recombinase expression is

Department of Clinical Neurobiology at the Medical Faculty of Heidelberg University and German Cancer Research Center (DKFZ), Heidelberg, Germany. Correspondence should be addressed to H.M. (h.monyer@dkfz-heidelberg.de).

Received 22 March 2013; accepted 11 March 2014; published online 6 April 2014; doi:10.1038/nn.3696

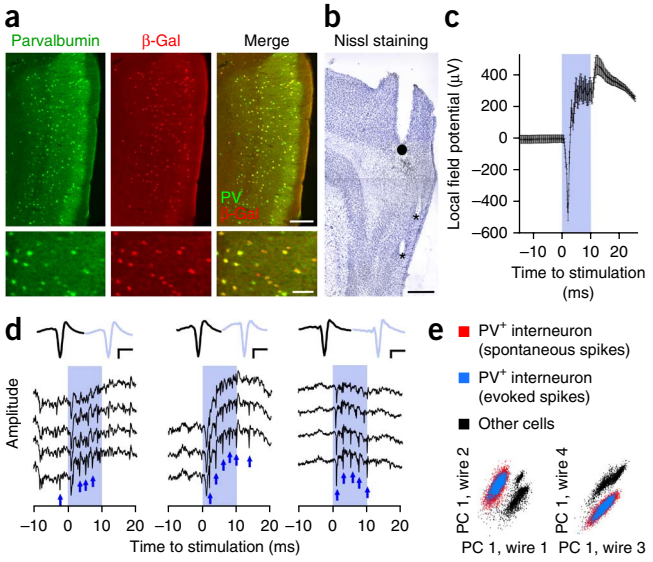


**Figure 1** Cell type–specific expression of ChR2-mCherry in PV+ interneurons of the MEC. (**a**) Immunostaining against parvalbumin and β-galactosidase (β-Gal) in 50-μm-thick sagittal sections of *PV-Cre–ROSA26* reporter mice and a merged image. Scale bars, 200 μm (top, ×4 magnification) and 50 μm (bottom, ×20 magnification). (**b**) Sagittal section stained with cresyl violet showing tetrode tracks (asterisks) reaching the superficial layers of the MEC. Black dot indicates optic fiber tip. Scale bar, 200 μm. (**c**) Local field potential (mean ± s.e.m.) from tetrodes that recorded grid cells ($n$ = 115 traces) in the MEC during laser stimulation (blue). (**d**) Mean spike waveforms (top) of three neurons calculated from spikes fired between laser stimulation periods (black) or during laser stimulation (blue). Scale bars, 1 ms and 50 μV. Examples of wide-band recordings from three tetrodes at the time of stimulation (bottom; blue area). Arrows indicate spikes. (**e**) Three spike clusters recorded on the same tetrode. Spikes from a neuron increasing its firing rate during laser stimulation are shown. The spontaneous spikes occurred between stimulation pulses and evoked spikes occurred during stimulation pulses. PC, principal component.

controlled by the parvalbumin promoter. We assessed the specificity of Cre recombinase expression in the MEC of *PV-Cre* mice in offspring obtained by breeding *PV-Cre* mice with *ROSA26* reporter mice[28]. In the MEC of *PV-Cre–ROSA26* mice, 92% of β-galactosidase+ neurons also expressed PV (**Fig. 1a**, 7 hemispheres from 4 mice, 5,863 cells counted in 44 slices; see **Supplementary Fig. 1** for a layer-specific quantification). To exclude the possibility of Cre recombinase–independent expression of ChR2-mCherry, we injected the virus into wild-type mice. We detected no mCherry-positive cells 14 d after injection (data not shown). In *PV-Cre* mice, PV+ interneurons expressing mCherry-ChR2 were present in all layers in the dorsal portion of the MEC and a dense plexus of labeled neurites was visible in layer II and III of the MEC (**Fig. 1a** and **Supplementary Fig. 1**).

We recorded single-unit activity and local field potentials in 12 adult mice expressing ChR2-mCherry in PV+ interneurons of the MEC. We chronically implanted mice with microdrives containing up to five tetrodes together with an optic fiber (**Supplementary Fig. 2a**). We confirmed tetrode location postmortem in Nissl-stained sagittal sections of the parahippocampal region (**Fig. 1b**). In most cases the final location of the tetrode tips was in layer II of the MEC.

To identify PV+ interneurons, we delivered pulses of blue light (473 nm, 10 ms) at a mean frequency of 6.67 Hz for 20 min. Light pulses caused an abrupt negative wave in the local field potential followed by a positive plateau (**Fig. 1c**). Whereas the negative component is a consequence of cation influx into PV+ interneurons[27], the positive plateau most likely represents inhibitory currents into cells receiving GABAergic synapses from PV+ interneurons[25]. We did not observe this biphasic field potential change when we delivered light stimulation in mice without expression of ChR2-mCherry (data not shown). In ChR2-mCherry–expressing mice, laser stimulation evoked spiking activity in neurons expressing ChR2-mCherry (**Fig. 1d**). Spike waveforms recorded during stimulation with light had very similar shapes to those recorded during the rest of the recording session, which allowed the identification of responding interneurons (**Fig. 1d**,**e** and **Supplementary Fig. 3a**,**b**). We classified as PV+ interneurons neurons that upon stimulation with light increased their firing rate at least 6 s.d. above baseline within 4 ms. Of all neurons recorded in the MEC, we identified 12.3% (140 of 1,134) as PV+ interneurons (**Fig. 2a**,**b** and **Supplementary Fig. 4**). Neurons that were not classified as PV+ interneurons showed either no change or a decrease in firing rate upon stimulation with light (**Fig. 2c**). The mean baseline firing rate of PV+ interneurons was 12.4 ± 1.2 Hz (mean ± s.e.m.) and increased to 49.4 ± 6.4 Hz during stimulation (**Fig. 2d**, Wilcoxon signed-rank test ($V$) = 994, $P = 2.3^{-11}$). The response firing rate of PV+ interneurons positively correlated with laser intensity (**Supplementary Fig. 2b–e**, Friedman test, $\chi^2 = 33.5$, $P < 0.0001$). The firing rate of neurons that were not classified as PV+ interneurons decreased from 5.8 ± 0.4 Hz to 3.8 ± 0.3 Hz during stimulation (**Fig. 2d**, $V$ = 477,678, $P < 2.2^{-16}$).

## Firing characteristics of PV+ interneurons

We first investigated how the spike waveform of PV+ interneurons differed from that of other neurons in the MEC (**Fig. 3a**). The trough-to-peak duration of spikes was shorter for PV+ interneurons (**Fig. 3a**,**b**, PV+: 0.328 ± 0.016 ms, other: 0.445 ± 0.006 ms, Wilcoxon rank-sum test, ($W$) = 42,616, $P = 5.96^{-14}$). The total spike width of PV+ interneurons was also significantly narrower than that of other neurons (PV+: 0.268 ± 0.005 ms, other: 0.289 ± 0.002 ms, $W$ = 56,785, $P = 4.0^{-4}$). The peak amplitude asymmetry of the spike waveform was more negative in PV+ interneurons (**Fig. 3c**, PV+: −0.450 ± 0.036 μV, other: 0.047 ± 0.014 μV, $W$ = 26,977, $P < 2.2^{-16}$). The spike amplitude was marginally larger in PV+ interneurons (PV+: 140.63 ± 5.56 μV, other: 130.36 ± 2.27 μV, $W$ = 76,843.5, $P$ = 0.048). The narrower waveform of PV+ interneurons compared to other neurons suggests that they are fast-spiking interneurons[21,22,29,30].

As the firing of most MEC neurons exhibits spatial selectivity, we characterized the activity of PV+ interneurons with respect to the position of the animal. Although the majority of neurons recorded in the MEC had firing fields limited to well-defined regions of the environment, most PV+ interneurons fired throughout the 70 cm × 70 cm open-field arena (**Fig. 3d** and **Supplementary Figs. 4** and **5**). PV+ interneurons had a higher firing rate and a lower sparsity score than other neurons during exploratory trials (**Fig. 3e**,**f**, median, firing rate, PV+: 15.60 Hz, other: 2.04 Hz, $W$ = 106,931, $P < 2.2^{-16}$, sparsity score, PV+: 0.071, other: 0.385, $W$ = 30,863, $P < 2.2^{-16}$). Like for most neurons in the MEC, the firing rate of PV+ interneurons was modulated by running speed (**Fig. 3g**). To assess the effect of speed on firing rate, we calculated the firing rate of cells for different running speed intervals. We normalized the firing rate in each interval to the firing rate of the cells when the animal had a low running speed (<5 cm $s^{-1}$). An analysis of variance (ANOVA) revealed that PV+ interneurons and other cells were similarly affected by running speed (main effect of speed: $F_{4,5,984}$ = 193.030, $P < 2.2^{16}$, cell-type × speed interaction: $F_{4,5,984}$ = 0.66, $P$ = 0.617). However, the normalized firing rate of PV+ interneurons was slightly higher than that of other neurons (main effect of cell type: $F_{1,1,496}$ = 7.911,

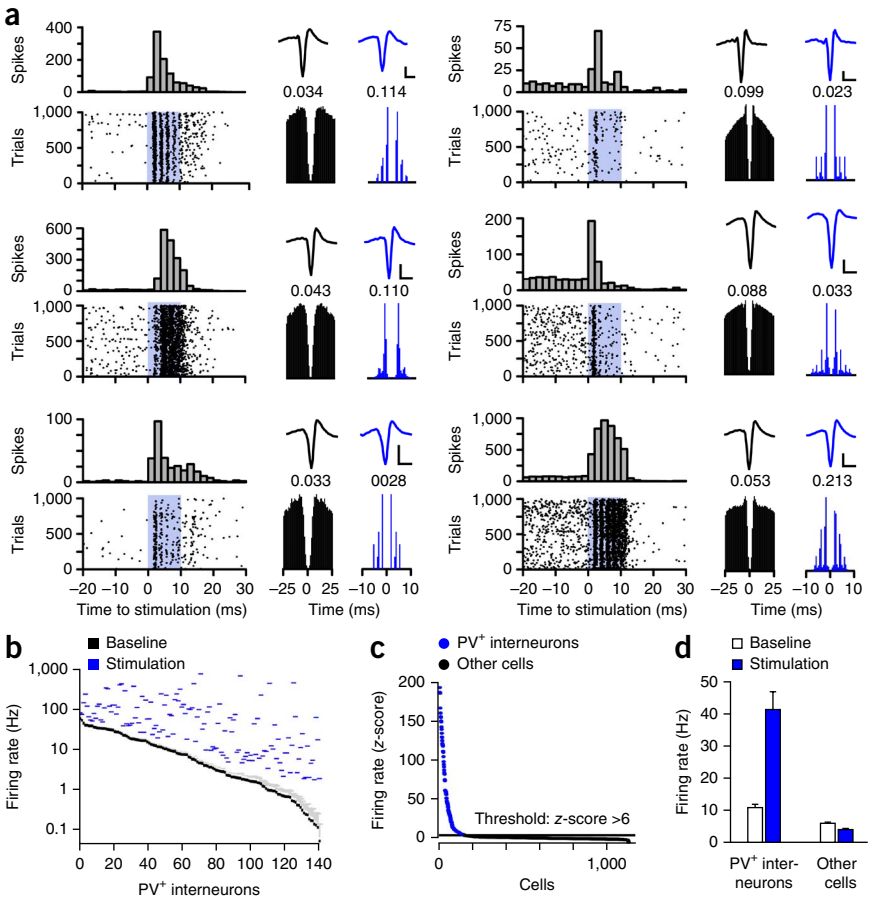


**Figure 2** Identification of PV+ interneurons in *PV-Cre* mice. (**a**) Peristimulation spike-count histograms and raster plots for six neurons that increased their firing rate upon stimulation (left). Mean spike waveform of the spikes from the tetrode wire recording the largest spike amplitude, occurring between (black) and during (blue) stimulation (top right in data for each of the six neurons). Scale bars, 0.5 ms, 50 μV. Spike-time autocorrelation for spikes occurring between (black) and during (blue) stimulation (bottom right). (**b**) Firing rate (mean ± s.d.) of PV+ interneurons during 50 ms preceding laser onset (baseline, calculated on 1-ms bins) and peak firing rate reached during the first 5 ms after laser onset. (**c**) Peak firing rate reached during the first 5 ms of laser stimulation expressed as a *z*-score from the firing rate preceding laser onset (baseline) for all recorded neurons. Cells with a *z*-score larger than 6 were classified as PV+ interneurons. Data for eight PV+ interneurons with a *z*-score > 200 are not displayed for illustrative reasons. (**d**) Firing rate of PV+ interneurons (mean ± s.e.m.) and other cells between (baseline) and during laser stimulation. For **b**–**d**, PV+ interneurons, $n = 140$ cells from 9 mice and other cells, $n = 994$ cells from 12 mice.

$P = 0.005$), which indicated that the firing rate increase from near immobility to periods of active exploration was slightly larger for PV+ interneurons than for other neurons.

To investigate whether the firing rate of PV+ interneurons encoded spatial information, we tested whether their firing-rate maps were stable during a 20 min exploratory trial in the open field. We computed firing-rate maps for the first and second half of the trial, and estimated map stability by performing a bin-by-bin correlation between the two maps for each PV+ interneuron. As control, we shifted spike trains along the mouse's path by a random interval of at least 20 s in each half of the trial and calculated map stability. We found that the stability of the spatial firing pattern of PV+ interneurons was significantly higher than chance (**Fig. 3h**, mean ± s.e.m., correlation coefficient, PV+: 0.376 ± 0.020, control: 0.031 ± 0.010, $W = 18{,}006.5$, $P < 2.2^{-16}$). Map stability of PV+ interneurons was, however, significantly below that of other cells of the MEC (correlation coefficient, other: 0.501 ± 0.009, $W = 50{,}056$, $P = 6.31^{-8}$). One possible confound is that map stability in PV+ interneurons resulted from differences in mean running speed across different regions of the open field. We controlled for this possibility by calculating the mean running speed of the mouse in each pixel of the firing-rate map for the entire 20 min trial. We used partial correlation analysis to determine whether the firing map was stable within a trial when we removed the effect of running speed. Map stability for PV+ interneurons after controlling for the potential effect of running speed was still significantly higher than chance level (correlation coefficient, PV+: 0.361 ± 0.020, $W = 17{,}761$, $P < 2.2^{-16}$).

Next, we categorized the recorded cells into functionally defined cell groups in the MEC (**Table 1** and **Fig. 3i**)[1,5,6]. We assigned neurons as being highly spatially selective if they showed high spatial sparsity or head-direction selectivity. Highly spatially selective cells included grid cells, border cells, head-direction cells, unclassified spatial cells, cells with characteristics of grid cells and head-direction cells (here referred to as grid–head-direction cells), and cells with characteristics of unclassified spatial cells and head-direction cells (unclassified spatial–head-direction cells; **Table 1**). We assigned every cell to only one class. We classified 64% of all recorded neurons as being highly spatially selective; of these only 3% were PV+ interneurons. Conversely, most PV+ interneurons (82%) were assigned to the cell category with low spatial selectivity. PV+ interneurons and other cells of the MEC distributed differently between the two cell categories (Pearson's $\chi^2$ test, $\chi^2 = 142$, $P < 2.2^{-16}$). This indicates that PV+ interneurons represent a prominent proportion of MEC neurons with low spatial selectivity.

We analyzed whether some PV+ interneurons displayed the spatial periodicity of grid cells or grid–head-direction cells. We calculated spatial autocorrelations of firing-rate maps for PV+ interneurons and grid cells (**Fig. 4a**, and **Supplementary Figs. 4** and **5**). Although grid cells showed a clear tessellating pattern in their firing-rate maps, the vast majority of PV+ interneurons did not display such an arrangement. In fact, these two cell types formed almost entirely non-overlapping populations when considering their spatial sparsity and grid score (**Fig. 4b**, grid score: PV+: 0.04 ± 0.02, grid cells: 0.60 ± 0.03, $W = 2{,}002$, $P < 2.2^{-16}$, spatial sparsity: PV+: 0.15 ± 0.04, grid cells: 0.51 ± 0.01, $W = 1{,}798$, $P < 2.2^{-16}$). To confirm the lack of regularity in the firing-rate maps of PV+ interneurons, we rotated their spatial autocorrelation maps by different degrees and calculated a correlation coefficient between the rotated and the original autocorrelation map. As expected, grid cells showed highly positive correlation coefficients at 60° and 120°, and negative coefficients at 30°, 90° and 150° (**Fig. 4c**). This pattern was absent in PV+ interneurons. We obtained similar results when we limited the analysis to PV+ interneurons recorded

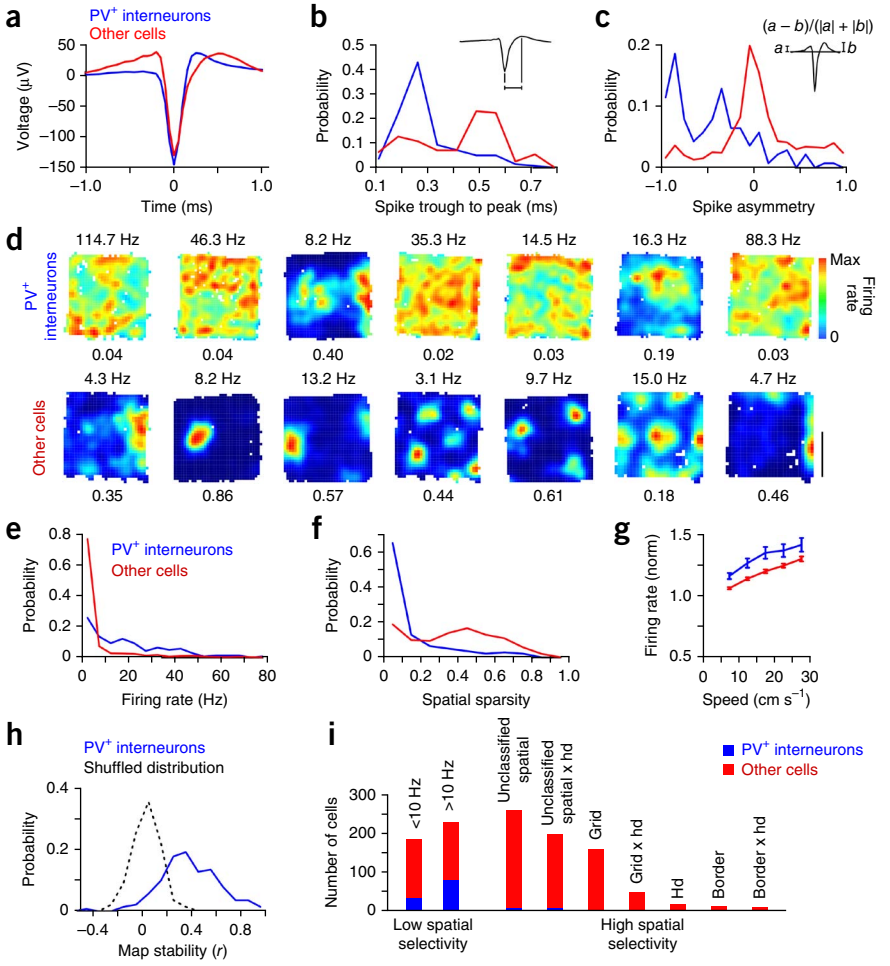


**Figure 3** Firing characteristics of PV+ interneurons. (**a**) Mean spike waveform (bandpass filter, 0.5–5 kHz) for PV+ interneurons and other cells recorded in the MEC. (**b**) Width of the raising phase of spikes (from trough to subsequent peak) for PV+ interneurons and other neurons. (**c**) Spike asymmetry in PV+ interneurons and other neurons. (**d**) Examples of 7 firing-rate maps from PV+ interneurons and 7 maps from other neurons that do not respond to light. Scale bar, 40 cm. Peak firing rates and grid scores are indicated above and below the firing-rate maps, respectively. (**e**) Mean firing rate of PV+ interneurons and other neurons during exploratory trials without laser stimulation. (**f**) Spatial sparsity of the firing maps for PV+ interneurons and other neurons in the open field arena without laser stimulation. (**g**) Normalized firing rate (mean ± s.e.m.) of PV+ interneurons and other cells with respect to running speed in the open field without laser stimulation. (**h**) Map stability of PV+ interneurons compared to that obtained after shifting the spike time on the path of the mouse (shuffled distribution). (**i**) Classification of MEC neurons based on their firing rate, spatial sparsity score, head-direction (hd) selectivity, grid score and border score. Most PV+ interneurons were classified as cells with a low spatial selectivity. 'x' indicates the presence of the two characteristics in the same cell. For **a**–**c**,**e**–**i**: PV+ interneurons, $n = 140$ cells from 9 mice; other cells, $n = 994$ cells from 12 mice.

simultaneously with grid cells on the same tetrode (**Supplementary Fig. 6a**). When we repeated the analysis with neurons with a high firing rate (putative interneurons, firing rate > 10 Hz), those data clearly deviated from that for grid cells and showed no periodic pattern in the spatial autocorrelation (**Supplementary Figs. 6b**,**c** and **7**).

### PV+ interneurons provide rapid inhibition to most MEC cells

We determined which neurons were inhibited by PV+ interneurons in the MEC network by studying the effect of activation of PV+ interneurons on the firing rate of other cell types (**Table 1**). Delivery of short (10 ms) light pulses at a mean frequency of 6.67 Hz led to robust silencing of neurons of every cell type (**Fig. 5a**). On average, neurons of all types showed a significant reduction in firing rate upon activation of PV+ interneurons (**Fig. 5b**, grid cells: $V = 11{,}771$, $P < 2.2^{-16}$, grid–head-direction cells: $V = 1{,}163$, $P = 4.0^{-7}$, unclassified spatial cells: $V = 31{,}042$, $P < 2.2^{-16}$, unclassified spatial–head-direction cells: $V = 16{,}598$, $P < 2.2^{-16}$, border cells: $V = 336$, $P = 4.1^{-6}$, interneurons with a high firing rate: $V = 10{,}916$, $P < 2.2^{-16}$). Postsynaptic cells recovered from inhibition 25 ms after the end of the laser pulse (spatially selective cells: 50% recovery from inhibition, **Fig. 5c**), which is consistent with the kinetics of $GABA_A$ receptors[25]. We considered single cells inhibited by PV+ interneurons if their firing rate decreased more than 2 s.d. from baseline during the light pulse. 71% of all cells were inhibited upon activation of PV+ interneurons (**Fig. 5d**). Cells inhibited by PV+ interneurons were distributed equally among the different cell types of the MEC (**Fig. 5d**, $\chi^2 = 130$, $P = 0.09$).

A short latency (<5 ms) between activation of PV+ interneurons and subsequent inhibition of postsynaptic cells suggests a monosynaptic connection, whereas a longer latency (>5 ms) argues in favor of pathways involving two or more synapses. PV+ interneurons were activated 1.42 ± 0.07 ms after the onset of photostimulation and the mean latency to inhibition of spatially selective cells was 3.29 ± 0.07 ms after the onset of photostimulation (**Fig. 5e**). The onset of PV+ interneuron–mediated inhibition in postsynaptic cells after on average less than 2 ms is in accordance with similar data obtained *in vitro*[25], and suggests monosynaptic connectivity between PV+ interneurons and the inhibited cells.

**Table 1 Criteria of ten functional cell types**

| Spatial selectivity | Cell type | Criteria | | | | |
|---|---|---|---|---|---|---|
| | | S | G | Hd | B | F |
| Low | High firing rate cells | | | | | x |
| | Low firing rate cells | | | | | |
| High | Unclassified spatial cells | x | | | | |
| | Unclassified spatial–head-direction cells | x | | x | | |
| | Grid cells | x | x | | | |
| | Grid–head-direction cells | x | x | x | | |
| | Head-direction cells | | | x | | |
| | Border cells | x | | | x | |
| | Border–head-direction cells | x | | x | x | |
| | High firing rate–head-direction cells | | | x | | x |

S, spatial sparsity score >0.8; G, grid score >0.3; Hd, head-direction score >0.3; B, border score >0.5; F, mean firing rate >10 Hz. A cell can only be assigned to one cell type. To be part of one cell type, a cell needs to meet all criteria of the cell type. If a cell meets all criteria of more than one cell type, it is assigned to the cell type with which it has the largest number of criteria in common.

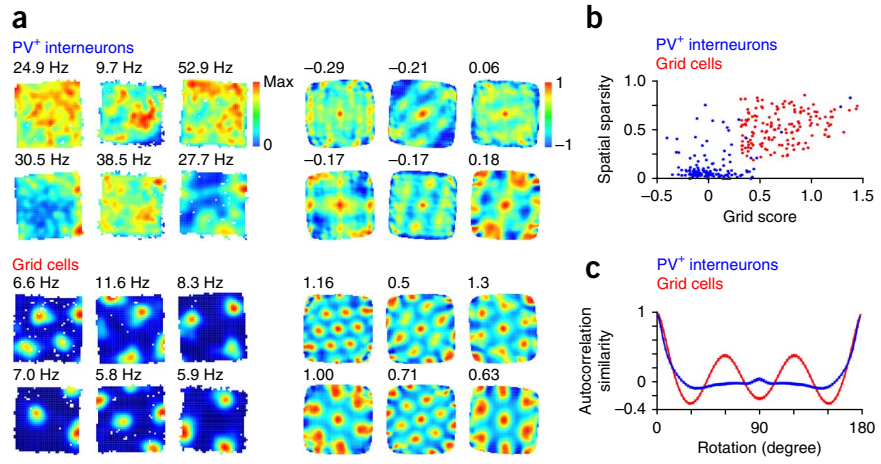


**Figure 4** Absence of grid-cell pattern in the firing of PV+ interneurons. (**a**) Firing-rate maps and spatial autocorrelations of 6 PV+ interneurons and 6 grid cells. Spatial autocorrelations of PV+ interneurons do not exhibit a hexagonal pattern. Peak firing rates and grid scores are displayed above the firing-rate maps and spatial autocorrelations, respectively. (**b**) Spatial sparsity and grid score for PV+ interneurons and grid cells. (**c**) Similarity of the spatial autocorrelation map with a rotated copy of itself (mean ± s.e.m.). PV+ interneurons do not show any clear periodicity. For **a**,**b**: PV+ interneurons, $n = 140$ cells from 9 mice; other cells, $n = 994$ cells from 12 mice.

### Spatial selectivity after activation of PV+ interneurons

To examine how PV+ interneuron–mediated inhibition affects functional characteristics of spatially selective cells in the MEC, we stimulated PV+ interneurons during spatial navigation. During foraging trials, we detected theta oscillation and triggered laser stimulation either at the trough or the peak of ongoing theta oscillation (**Fig. 6a** and **Supplementary Fig. 8**). When we stimulated at the peak of theta oscillation, cells with a grid-cell pattern (grid cells and grid–head-direction cells) decreased their firing rate from 1.43 ± 0.13 Hz during sham stimulation to 1.08 ± 0.12 Hz during laser stimulation ($V = 409$, $P = 7.0^{-5}$). When we stimulated at the trough of theta oscillation, the firing rate decreased from 1.52 ± 0.16 Hz to 0.87 ± 0.12 Hz (**Fig. 6b**, $V = 458$, $P = 1.2^{-7}$). Similarly, head-direction cells (unclassified spatial–head-direction cells and head-direction cells) reduced their firing rate from 1.91 ± 0.18 Hz to 1.36 ± 0.15 Hz ($V = 644$, $P = 2.8^{-8}$) during peak stimulation, and from

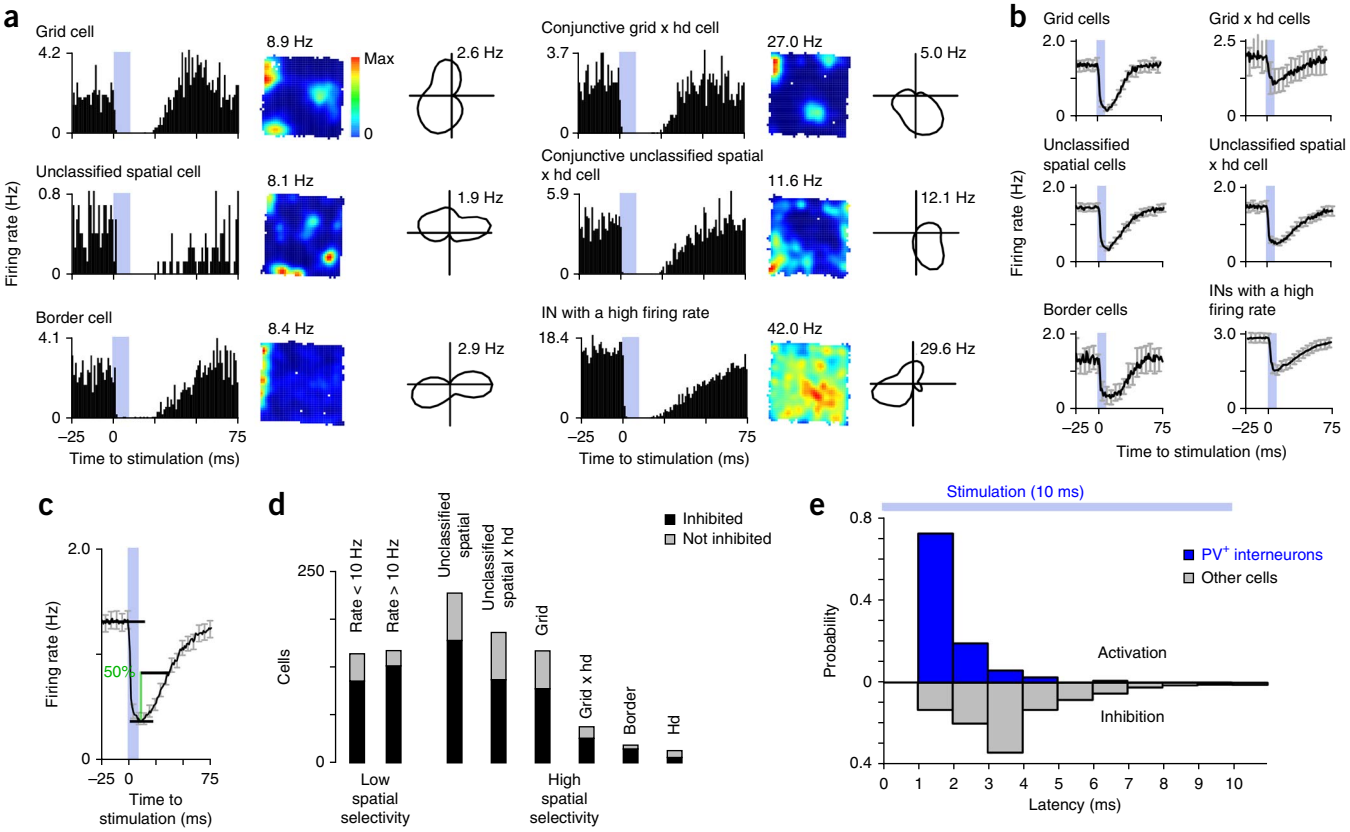


**Figure 5** Inhibition of spatially selective cells by PV+ interneurons. (**a**) Examples of spatially selective cells and an interneuron with a high firing rate inhibited during 10 ms stimulation with light delivered at a mean frequency of 6.67 Hz. From left to right: peristimulation histogram, spatial firing map and polar plot showing head-direction selectivity. Numbers above the firing-rate map and polar plot indicate peak firing rates. (**b**) Mean peristimulation histogram (mean ± s.e.m.) for distinct groups of cells recorded in the MEC ($n = 158$ grid cells, 249 unclassified spatial cells, 17 border cells, 50 grid–head-direction (hd) cells, 189 unclassified spatial–head-direction cells, 149 interneurons with a high firing rate from 12 mice). 'x' indicates the presence of the two characteristics in the same cell. IN, putative interneuron. (**c**) Mean peristimulation histogram (mean ± s.e.m.) for all spatially selective cells ($n = 720$ cells from 12 mice). (**d**) Proportion of cells of distinct groups that were inhibited after laser stimulation. (**e**) Onset of activation in PV+ interneurons ($n = 140$ cells from 9 mice) and inhibition in other cells ($n = 994$ from 12 mice) upon stimulation with light.

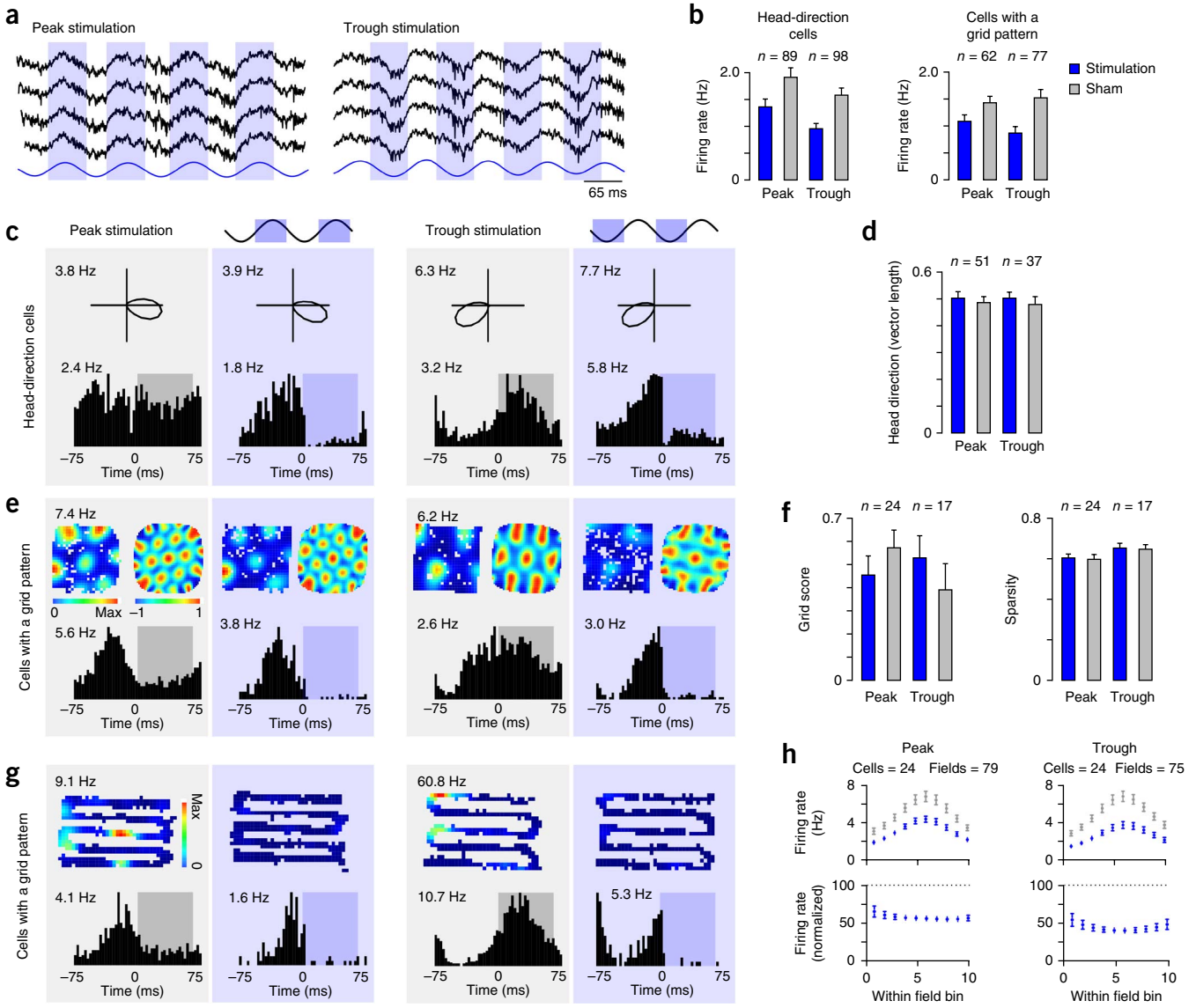


**Figure 6** Theta phase–specific stimulation of PV+ interneurons inhibits MEC neurons without affecting their spatial selectivity. (**a**) PV+ interneuron activation (blue shading) at the peak or trough of theta oscillation. Wide-band recordings and filtered signal (blue lines) from two tetrodes. (**b**) Firing rate (mean ± s.e.m.) of head-direction cells (unclassified spatial–head-direction cells and head-direction cells) and cells with a grid-cell pattern (grid cells and grid–head-direction cells) upon peak or trough stimulation. (**c**) Data for two head-direction cells upon peak or trough stimulation. Polar plot indicates the head-direction preference of cells. Peristimulation histogram shows inhibition of cells during laser stimulation (blue area) or sham stimulation (gray area). Background shading indicates data collected during laser stimulation (blue outline) and sham stimulation (gray outline). (**d**) Head-direction selectivity (mean ± s.e.m.) of two head-direction cells during stimulation. (**e**) Spatial firing-rate map and spatial autocorrelation (top) for two cells with a grid pattern upon peak (left) or trough stimulation (right). Peak firing rates for maps of the same cell are indicated. Color bar below firing-rate map indicates firing rate. Color bar below spatial autocorrelation indicates correlation coefficient. Peristimulation histograms show inhibition of cells upon laser stimulation (blue area) or sham stimulation (gray area). (**f**) Grid score and spatial sparsity (mean ± s.e.m.) of cells with a grid-cell pattern during stimulation. (**g**) Firing rate of two cells with a grid-cell pattern as the mouse ran in the zigzag maze. Peristimulation histogram shows inhibition of cells upon laser stimulation (blue area) or sham stimulation (gray area). (**h**) Firing rate (top, mean ± s.e.m.) within place fields during peak (left) and trough (right) stimulation. Firing rate normalized to sham stimulation throughout the place field (bottom).

1.58 ± 0.13 Hz to 0.95 ± 0.10 Hz during trough stimulation (**Fig. 6b**, $V = 726$, $P = 1.7^{-9}$). To control for the reduction in firing rate upon laser stimulation, we down-sampled the number of spikes during sham stimulation accordingly, and we only included cells for further analysis that still had a grid score or head-direction selectivity above threshold (grid score = 0.3, head-direction vector length = 0.3). Despite a clear reduction in firing rate, head-direction cells maintained their head-direction preference (**Fig. 6c**,**d**, head-direction selectivity (vector length), peak stimulation, sham: 0.49 ± 0.02, laser: 0.50 ± 0.02, $V = 801$, $P = 0.2$, trough stimulation, sham: 0.48 ± 0.03, laser: 0.50 ± 0.02, $V = 445$, $P = 0.16$). Similarly, cells with a grid-cell pattern kept their grid-cell periodicity and spatial sparsity during theta phase–specific stimulation (**Fig. 6e**,**f**, grid score, peak stimulation, sham: 0.57 ± 0.08, laser: 0.46 ± 0.08, $V = 119$, $P = 0.39$, trough stimulation, sham: 0.39 ± 0.11, laser: 0.53 ± 0.1, $V = 96$, $P = 0.38$, spatial sparsity, peak stimulation, sham: 0.595 ± 0.024, laser: 0.603 ± 0.018, $V = 331$, $P = 0.58$, trough stimulation, sham: 0.646 ± 0.023, laser: 0.651 ± 0.024, $V = 152$, $P = 0.69$).

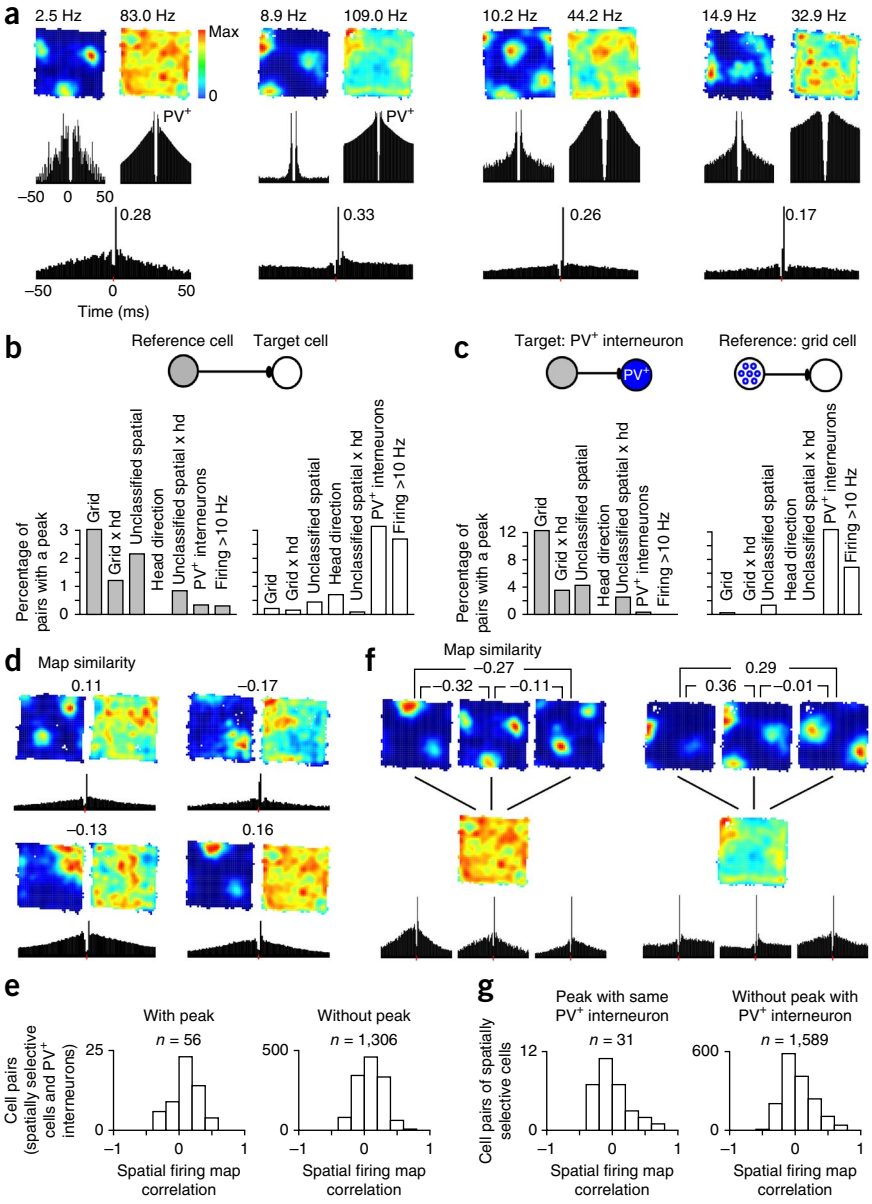


**Figure 7** Connectivity between excitatory cells and PV+ interneurons. (**a**) Firing-rate maps and spike-time autocorrelations for pairs of spatially selective cells (reference cell, left) and interneurons (target cell, right) with a peak at short latency in their cross-correlogram. Bottom, spike-time cross-correlation between reference and target neuron. Time 0 indicates a spike of the reference neuron. (**b**) Percentage of cross-correlograms with a peak for pairs of different cell types as reference or target neurons. (**c**) Percentage of cross-correlograms with a peak at short latency with PV+ interneurons as target neurons (left) or grid cells as reference neurons (right). (**d**) Similarity between maps of four cell pairs, each consisting of a spatially selective neuron (left) with a PV+ interneuron (right) that show a peak in their cross-correlogram. Similarity scores are provided above the maps. Bottom, spike-time cross-correlation between the reference and the target neuron. (**e**) Map similarity for pairs of spatially selective cells and PV+ interneurons with (left) and without (right) a peak in their cross-correlogram. (**f**) Two PV+ interneurons with peaks in their cross-correlograms with several grid cells. Similarity scores between grid-cell maps are shown. Bottom, spike-time cross-correlation between each grid cell and the PV+ interneuron. Grid cells with different phases have peaks in their cross-correlogram with a common PV+ interneuron. (**g**) Map similarity between cell pairs with a peak in their cross-correlogram of spatially selective cells and a common PV+ interneuron (left), and pairs with no peak in their cross-correlogram of spatially selective cells with a PV+ interneuron (right).

To analyze the effect of PV+ interneuron–mediated inhibition on single place fields in more detail, we recorded the activity of neurons in mice running in a zigzag maze. This procedure constrained the mouse to a single movement path and simplified place-field analysis (**Fig. 6g**). We divided place fields into ten bins and aligned place fields to the running direction. Independently of stimulation phase, cells with a grid-cell pattern exhibited a reduced peak firing rate in their place fields during laser stimulation (**Fig. 6h**, peak firing rate, peak stimulation, $n = 91$ place fields, sham: $7.65 \pm 0.57$ Hz, laser: $5.09 \pm 0.38$ Hz, $V = 3{,}566$, $P = 5.6^{-9}$, trough stimulation, $n = 102$ place fields, sham: $7.73 \pm 0.59$ Hz, laser: $4.32 \pm 0.36$ Hz, $V = 4{,}336$, $P = 1.2^{-8}$). To investigate the inhibition of cells with a grid-cell pattern at different locations in the place fields, we selected only place fields that showed a reduced mean firing rate during laser stimulation (percentage of place fields that were inhibited, peak stimulation: 82%, trough stimulation: 77%). A two-way ANOVA (position × stimulation phase) showed that stimulation of PV+ interneurons at the trough of theta oscillation had a larger effect on the normalized firing rate in the place field (**Fig. 6h**, main effect of stimulation phase: $F_{1,152} = 8.92$, $P = 0.003$). However, the change in firing rate was similar throughout the place field (**Fig. 6h**, main effect of position: $F_{9,1368} = 1.55$, $P = 0.12$, position × stimulation-phase interaction: $F_{9,1368} = 1.88$, $P = 0.05$).

### Recruitment of PV+ interneurons by excitatory cells

PV+ interneurons in the CA1 region of the hippocampus receive strong excitatory connections from adjacent neurons[30]. We used spike-time cross-correlograms from simultaneously recorded neurons to probe for excitatory connectivity onto PV+ interneurons. As previously proposed, a peak at short latency in the cross-correlogram is likely to reflect a monosynaptic excitatory connection[30–32]. However, one cannot exclude with certainty the possibility that some peaks at short latency might arise from a common synaptic input with different latencies onto simultaneously recorded neurons. We tested a total of 12,952 cross-correlograms, of which 163 (1.3%) had a peak at short latency (6 s.d. above baseline, < 4 ms, **Fig. 7a** and **Supplementary Fig. 9a–d**). The probability for a significant peak in the cross-correlogram for pairs of cells recorded on the same tetrode was higher than for pairs recorded on different tetrodes (same tetrode: 133/3,538 pairs, different tetrodes: 30/9,414 pairs, $\chi^2 = 22{,}904$, $P < 2.2^{-16}$). We calculated the probability that a neuron belonging to a given cell type had a significant peak in its cross-correlograms, when acting as a reference neuron to all other target neurons. We excluded border cells from this analysis because our recordings comprised only few cells of this type. Among all spatially selective cell types, grid cells were most likely to show peaks in their cross-correlograms, followed

by unclassified spatial cells and grid–head-direction cells (**Fig. 7b** and **Supplementary Fig. 9a–d**, percentage of all cross-correlograms of a given cell type with a peak: grid cells: 3.0%, unclassified spatial cells: 2.1%, grid–head-direction cells: 1.2%). This difference could not be accounted for by a lower average firing rate of unclassified spatial cells and grid–head-direction cells compared to grid cells (**Supplementary Fig. 9k**). In most cases, the target neuron was either a $PV^+$ interneuron or an interneuron with high firing rate (**Fig. 7b**, percentage of all cross-correlograms with a target neuron of a given cell type, $PV^+$: 3.2%, interneurons with a high firing rate: 2.7%). Grid cells, unclassified spatial cells and grid–head-direction cells showed 67.7% of their peaks in cross-correlograms when the target neurons were $PV^+$ interneurons or other interneurons with a high firing rate. We observed the highest number of peaks in cross-correlograms between grid cells and $PV^+$ interneurons (12.3% pairs with a peak in the cross-correlogram, **Fig. 7c**). When considering only pairs of grid cells and $PV^+$ interneurons on the same tetrode, this percentage was 33% (same tetrode: 22/66 pairs, different tetrodes: 4/145 pairs, $\chi^2 = 300{,}404$, $P < 2.2^{-16}$). We observed only a single cross-correlogram with a peak among 334 pairs of simultaneously recorded grid cells, which likely reflects the low probability of connections between grid cells[21,22]. Overall, when detected, the spike probability of the peak remained stable for the time of a recording session as well as between brain states (**Supplementary Fig. 9e–j,l,m**).

The high percentage of cross-correlograms with a peak at short latency between grid cells and $PV^+$ interneurons indicates that $PV^+$ interneurons receive a strong excitatory drive from grid cells. Despite this putative connectivity, most $PV^+$ interneurons showed low sparsity and lacked spatial periodicity. We therefore investigated whether cells targeting $PV^+$ interneurons impose their spatial firing onto $PV^+$ interneurons. We compared map similarity between firing maps of pairs with a peak in their cross-correlogram to that of pairs with no peak (**Fig. 7d,e**). Only pairs in which the reference neuron was highly spatially selective and the target neuron was a $PV^+$ interneuron were considered. Map similarity for pairs with and without a significant peak in their cross-correlograms did not differ (**Fig. 7e**, $n = 56$ pairs with a peak, correlation coefficient: $0.11 \pm 0.03$, $n = 1{,}306$ pairs without a peak, correlation coefficient: $0.10 \pm 0.005$, $W = 38{,}891$, $P = 0.42$, **Supplementary Fig. 10**). The small shift toward positive values was most likely due to systematic variations within recording sessions as we did not observe it in pairs of cells for which the pair members were recorded in different sessions (**Supplementary Fig. 10e–h**). This indicates that a single reference neuron did not impose its spatial firing pattern onto the target $PV^+$ interneuron. The apparent lack of influence of the reference neuron on the spatial firing of $PV^+$ interneurons suggests that cells with putative excitatory connections onto the same target $PV^+$ interneuron have diverging spatial firing patterns. We tested this hypothesis by comparing the spatial firing-rate map of spatially selective cells that showed a peak in their cross-correlogram with a common $PV^+$ interneuron (**Fig. 7f**). We found that grid cells with different phases have peaks in their cross-correlogram with the same $PV^+$ interneuron. Map similarity for pairs of spatially selective cells exhibiting a peak at short latency with a common $PV^+$ interneuron was not higher than for pairs of spatially selective cells that had no peak in their cross-correlogram with a $PV^+$ interneuron (**Fig. 7f,g**, correlation coefficient, 31 pairs with peak: $0.00 \pm 0.05$, 1,589 pairs without peak: $0.05 \pm 0.006$, $W = 21{,}506$, $P = 0.23$, **Supplementary Fig. 10**). Moreover, the mean map similarity for pairs of spatially selective cells that showed a peak in their cross-correlogram with a shared $PV^+$ interneuron was not different from 0 (Student's $t$-test, $t = 0.08$, $P = 0.94$). These findings indicate that $PV^+$ interneurons continuously receive excitatory input from grid cells as an animal explores the environment. However, different neuronal ensembles provide depolarization depending on the exact location of the animal. It should be pointed out that the proposed connectivity scheme based on cross-correlation analysis warrants validation by other methods that allow unambiguous detection of monosynaptic connectivity, for example, paired-patch recordings.

## DISCUSSION

Our investigation of the firing properties and functional connectivity of $PV^+$ interneurons in the MEC network revealed the following. First, the firing of $PV^+$ interneurons was broadly tuned to position and did not exhibit grid-cell periodicity, yet it still contained information about the location of the animal. Second, $PV^+$ interneurons robustly inhibited the firing activity of all functionally defined cell types in the MEC. Although increased $PV^+$ interneuron–mediated inhibition was sufficient to reduce firing activity, it did not alter spatial selectivity of cells with a grid-cell pattern and head-direction cells. Third, $PV^+$ interneurons integrated excitatory inputs from grid cells with various phases.

$PV^+$ interneurons exhibited low spatial sparsity. This contrasts sharply with that of grid cells and grid–head-direction cells, which represent a large proportion of the neurons in the superficial layers of the MEC[33]. The low sparsity of $PV^+$ interneurons in the MEC is reminiscent of what has been reported for other brain regions. For instance, $PV^+$ interneurons are broadly tuned to the orientation of visual stimuli in the primary visual cortex[34,35] and to odors in the olfactory bulb[36,37]. Similarly, $PV^+$ interneurons in the hippocampus do not exhibit sharp place fields but fire throughout the environment[38]. Hence broad selectivity to sensory information appears to be one of the hallmarks of $PV^+$ interneurons in cortical areas. We found that the low spatial sparsity of $PV^+$ interneurons in the MEC very likely results from the strong excitation conveyed onto them by grid cells and grid–head-direction cells with various phases. Despite the low spatial sparsity, $PV^+$ interneurons exhibited stability in the firing-rate map. The spatial information in the firing-rate maps of $PV^+$ interneurons can be explained if taking into consideration that $PV^+$ interneurons integrate the inputs from multiple grid cells and that the peak firing rate of a grid cell typically varies across firing fields. Similarly, the running speed modulation of $PV^+$ interneurons could also be inherited from the integration of grid-cell inputs. It will be interesting to see whether the broad tuning of $PV^+$ interneurons in other brain regions can also be explained by similar network-organization priniciples.

Our results challenge current attractor-network models. In these models, inhibitory connectivity between grid cells is included and accounts for the observation that stellate cells in layer II are very sparsely connected[18,21,22,24]. The models demonstrate that phase-dependent recurrent inhibition between grid cells is sufficient to generate stable grid cell–like firing fields. This leads to the pressing question: which interneurons are the most likely to provide the inhibition that models rely on? The answer is $PV^+$ interneurons for the following reasons. First, $PV^+$ interneurons are the most abundant interneuron cell type in the superficial layers of the MEC[8,9]. Second, they make numerous synaptic contacts onto principal neurons[8,10–12]. Third, as we showed here, they are preferentially recruited by grid cells. However, and most importantly, the recruitment of individual $PV^+$ interneurons by grid cells with various phases argues against a scenario in which $PV^+$ interneurons provide phase-dependent recurrent inhibition.

By modeling explicitly inhibitory interneurons in their grid cell model, others have made clear predictions regarding the spatial firing patterns of inhibitory interneurons[22]. Thus, depending on the exact

weights of inhibitory and excitatory connections within the network, inhibitory interneurons have either normal or inverted grid cell–like firing fields. This, however, is not what we found, as PV$^+$ interneurons did not show a grid-cell pattern or inverted grid-cell pattern. This result lends credence to our hypothesis that PV$^+$ interneurons do not mediate phase-dependent recurrent inhibition to generate grid-cell periodicity. Furthermore, it argues against the notion that the summation of weak phase-dependent excitatory connections, which we could not detect under our recording conditions, may have an impact on PV$^+$ interneuron firing.

Hence other possibilities will have to be explored when considering the generation of the grid-cell firing pattern. For instance, it is conceivable that an attractor network which generates grid cell periodicity via recurrent excitatory connections between grid cells is located in layer III of the MEC. The high connection probability between excitatory cells reported there would support this scenario[23,39]. Of course, other brain areas that exhibit high recurrent connectivity and cells with grid-cell periodicity could accommodate the attractor network[40]. In such a case, PV$^+$ interneurons in the superficial layers of the MEC could control the gain of grid-cell output. This function is supported by our observation that increased PV$^+$ interneuron–mediated inhibition leads to a reduction of firing rate throughout the firing fields of grid cells. In the visual and olfactory cortex, PV$^+$ interneurons linearly transform the output of principal cells[34,36]. Thus, output gain control may be a general feature of PV$^+$ interneurons in several cortical circuits.

## METHODS

Methods and any associated references are available in the online version of the paper.

*Note: Any Supplementary Information and Source Data files are available in the online version of the paper.*


### ACKNOWLEDGMENTS

We thank E. Savenkova and U. Amtmann for their technical assistance, W. Kelsch for providing help at initial stages of the study, M. Michael for immunohistochemical work, and P. Latuske for help with pilot experiments. This work was supported by a Humboldt Research Fellowship for Postdoctoral Studies and a grant from the Innovation Fund FRONTIER of Heidelberg University to K.A., a grant from the European Research Council Advanced Grant (Proposal number 250047) to H.M., and a grant from the German Ministry for Education and Research (BMBF, 01GQ1003A).


### AUTHOR CONTRIBUTIONS

C.B., K.A. and H.M. designed the experiments and wrote the manuscript. C.B. and K.A. performed *in vivo* electrophysiological experiments. C.B and K.A. analyzed the data.

### COMPETING FINANCIAL INTERESTS

The authors declare no competing financial interests.




1. Hafting, T., Fyhn, M., Molden, S., Moser, M.-B. & Moser, E.I. Microstructure of aspatial map in the entorhinal cortex. *Nature* **436**, 801–806 (2005).
2. Taube, J.S., Muller, R.U. & Ranck, J. Jr. Head-direction cells recorded from the postsubiculum in freely moving rats. I. Description and quantitative analysis. *J. Neurosci.* **10**, 420–435 (1990).
3. O'Keefe, J. & Nadel, L. *The Hippocampus as a Cognitive Map* (Oxford University Press, Oxford, 1978).
4. Morris, R.G., Garrud, P., Rawlins, J.N. & O'Keefe, J. Place navigation impaired in rats with hippocampal lesions. *Nature* **297**, 681–683 (1982).
5. Sargolini, F. *et al.* Conjunctive representation of position, direction, and velocity in entorhinal cortex. *Science* **312**, 758–762 (2006).
6. Solstad, T., Boccara, C.N., Kropff, E., Moser, M.-B. & Moser, E.I. Representation of geometric borders in the entorhinal cortex. *Science* **322**, 1865–1868 (2008).
7. Jones, R.S. & Bühl, E.H. Basket-like interneurones in layer II of the entorhinal cortex exhibit a powerful NMDA-mediated synaptic excitation. *Neurosci. Lett.* **149**, 35–39 (1993).
8. Wouterlood, F.G., Härtig, W., Brückner, G. & Witter, M.P. Parvalbumin-immunoreactive neurons in the entorhinal cortex of the rat: localization, morphology, connectivity and ultrastructure. *J. Neurocytol.* **24**, 135–153 (1995).
9. Miettinen, M., Koivisto, E., Riekkinen, P. & Miettinen, R. Coexistence of parvalbumin and GABA in nonpyramidal neurons of the rat entorhinal cortex. *Brain Res.* **706**, 113–122 (1996).
10. Varga, C., Lee, S.Y. & Soltesz, I. Target-selective GABAergic control of entorhinal cortex output. *Nat. Neurosci.* **13**, 822–824 (2010).
11. Canto, C.B., Wouterlood, F.G. & Witter, M.P. What does the anatomical organization of the entorhinal cortex tell us? *Neural Plast.* **2008**, 381243 (2008).
12. Soriano, E., Martinez, A., Farinas, I. & Frotscher, M. Chandelier cells in the hippocampal formation of the rat: the entorhinal area and subicular complex. *J. Comp. Neurol.* **337**, 151–167 (1993).
13. Burgess, N., Barry, C. & O'Keefe, J. An oscillatory interference model of grid cell firing. *Hippocampus* **17**, 801–812 (2007).
14. Zilli, E.A. & Hasselmo, M.E. Coupled noisy spiking neurons as velocity-controlled oscillators in a model of grid cell spatial firing. *J. Neurosci.* **30**, 13850–13860 (2010).
15. Kropff, E. & Treves, A. The emergence of grid cells: intelligent design or just adaptation? *Hippocampus* **18**, 1256–1269 (2008).
16. McNaughton, B.L., Battaglia, F.P., Jensen, O., Moser, E.I. & Moser, M.-B. Path integration and the neural basis of the 'cognitive map'. *Nat. Rev. Neurosci.* **7**, 663–678 (2006).
17. Fuhs, M.C. & Touretzky, D.S. A spin glass model of path integration in rat medial entorhinal cortex. *J. Neurosci.* **26**, 4266–4276 (2006).
18. Burak, Y. & Fiete, I.R. Accurate path integration in continuous attractor network models of grid cells. *PLoS Comput. Biol.* **5**, e1000291 (2009).
19. Domnisoru, C., Kinkhabwala, A.A. & Tank, D.W. Membrane potential dynamics of grid cells. *Nature* **495**, 199–204 (2013).
20. Schmidt-Hieber, C. & Häusser, M. Cellular mechanisms of spatial navigation in the medial entorhinal cortex. *Nat. Neurosci.* **16**, 325–331 (2013).
21. Couey, J.J. *et al.* Recurrent inhibitory circuitry as a mechanism for grid formation. *Nat. Neurosci.* **16**, 318–324 (2013).
22. Pastoll, H., Solanka, L., van Rossum, M.C.W. & Nolan, M.F. Feedback inhibition enables theta-nested gamma oscillations and grid firing fields. *Neuron* **77**, 141–154 (2013).
23. Dhillon, A. & Jones, R.S. Laminar differences in recurrent excitatory transmission in the rat entorhinal cortex in vitro. *Neuroscience* **99**, 413–422 (2000).
24. Bonnevie, T. *et al.* Grid cells require excitatory drive from the hippocampus. *Nat. Neurosci.* **16**, 309–317 (2013).
25. Cardin, J.A. *et al.* Driving fast-spiking cells induces gamma rhythm and controls sensory responses. *Nature* **459**, 663–667 (2009).
26. Fuchs, E.C. *et al.* Recruitment of parvalbumin-positive interneurons determines hippocampal function and associated behavior. *Neuron* **53**, 591–604 (2007).
27. Nagel, G. *et al.* Channelrhodopsin-2, a directly light-gated cation-selective membrane channel. *Proc. Natl. Acad. Sci. USA* **100**, 13940–13945 (2003).
28. Soriano, P. Generalized lacZ expression with the ROSA26 Cre reporter strain. *Nat. Genet.* **21**, 70–71 (1999).
29. McCormick, D.A., Connors, B.W., Lighthall, J.W. & Prince, D.A. Comparative electrophysiology of pyramidal and sparsely spiny stellate neurons of the neocortex. *J. Neurophysiol.* **54**, 782–806 (1985).
30. Csicsvari, J., Hirase, H., Czurko, A. & Buzsáki, G. Reliability and state dependence of pyramidal cell-interneuron synapses in the hippocampus: an ensemble approach in the behaving rat. *Neuron* **21**, 179–189 (1998).
31. Marshall, L. *et al.* Hippocampal pyramidal cell-interneuron spike transmission is frequency dependent and responsible for place modulation of interneuron discharge. *J. Neurosci.* **22**, RC197 (2002).
32. Maurer, A.P., Cowen, S.L., Burke, S.N., Barnes, C.A. & McNaughton, B.L. Phase precession in hippocampal interneurons showing strong functional coupling to individual pyramidal cells. *J. Neurosci.* **26**, 13485–13492 (2006).
33. Stensola, H. *et al.* The entorhinal grid map is discretized. *Nature* **492**, 72–78 (2012).
34. Atallah, B.V., Bruns, W., Carandini, M. & Scanziani, M. Parvalbumin-expressing interneurons linearly transform cortical responses to visual stimuli. *Neuron* **73**, 159–170 (2012).
35. Zariwala, H.A. *et al.* Visual tuning properties of genetically identified layer 2/3 neuronal types in the primary visual cortex of cre-transgenic mice. *Front. Syst. Neurosci.* **4**, 162 (2011).
36. Kato, H.K., Gillet, S.N., Peters, A.J., Isaacson, J.S. & Komiyama, T. Parvalbumin-expressing interneurons linearly control olfactory bulb output. *Neuron* **80**, 1218–1231 (2013).
37. Miyamichi, K. *et al.* Dissecting local circuits: parvalbumin interneurons underlie broad feedback control of olfactory bulb output. *Neuron* **80**, 1232–1245 (2013).
38. Royer, S. *et al.* Control of timing, rate and bursts of hippocampal place cells by dendritic and somatic inhibition. *Nat. Neurosci.* **15**, 769–775 (2012).
39. Giocomo, L.M., Moser, M.-B. & Moser, E.I. Computational models of grid cells. *Neuron* **71**, 589–603 (2011).
40. Boccara, C.N. *et al.* Grid cells in pre- and parasubiculum. *Nat. Neurosci.* **13**, 987–994 (2010).

## ONLINE METHODS

**Virus preparation.** An adeno-associated viral (AAV) vector containing a double *loxP*-flanked (floxed) inverted open (DIO) reading frame coding for ChR2-mCherry (AAV DIO *ChR2-mCherry*) was obtained from K. Deisseroth (Stanford University)[25]. In the presence of Cre recombinase, the cassette containing *ChR2-mCherry* is inverted into the sense direction, and ChR2-mCherry is expressed from the *EF1* promoter. AAV chimeric vector (virions containing a 1:1 ratio of AAV1 and AAV2 capsid proteins with AAV2 ITRs) was generated as described previously[41]. HEK293 cells were transfected with the AAV cis plasmid, the AAV1 and AAV2 helper plasmids, and the adenovirus helper plasmid. 60 h after transfection, cells were harvested, and the vector was purified using heparin affinity columns (Sigma).

**Virus injection and microdrive implantation.** All mouse experiments were performed according to the guidelines for laboratory animal welfare (Regierungspräsidium Karlsruhe, license Az G-113/10). Experiments were conducted in 3–6-month-old male *PV-Cre* mice with a C57BL/6 background[26]. Mice were singly housed and kept on a 12 h light-dark schedule with all procedures performed during the light phase. Mice were anesthetized with isoflurane (1.0–2.5%), mounted in a stereotaxic apparatus and kept under isoflurane anesthesia during surgery. A craniotomy was made above the MEC. A glass micropipette containing the virus was inserted into the brain at a 9° angle in the anterior direction, 0.2 mm anterior from the transverse sinus and 3.1 mm lateral from bregma. The micropipette was lowered 1.8 mm below the brain surface, and the virus was injected (200–350 nl) over a period of 3 min. The micropipette was left in place for 8 min before retraction.

A microdrive holding 4–5 independently moving tetrodes and an optical fiber were chronically implanted with tetrodes directed at the MEC. The tetrodes were constructed from 12-µm-diameter tungsten wires (H-Formvar insulation with Butyral bond coat; California Fine Wire). The fiber optic patchcord consisted of a 100 µm multimode fiber core and 140 µm cladding assembled with a 900 µm loose jacket (Doric Lenses). The optic fiber was mounted into the microdrive so that the distance between the optical fiber and the closest tetrode was ~0.2–0.3 mm. The dura mater above the MEC was removed, and the tetrodes and the stripped tip of the optic fiber were inserted 0.8 mm into the brain above the MEC at a 6° angle in the posterior direction. Two stainless-steel screws were implanted into the bone above the cerebellum, and served as reference and ground signals.

**Electrophysiological recordings.** After a 1 week recovery period, the tetrodes were lowered into the MEC while the optic fiber stayed in place. Tetrodes were considered to be located in the MEC based on the occurrence of large theta oscillations, a strong theta modulation of action potentials and the presence of grid cells. Tetrode placement was subsequently confirmed by histological analysis. After each recording session, the tetrodes were moved down by 25–50 µm. For most recordings tetrode tips and optic fiber tip were expected to be 1–2 mm apart. Channel unity-gain preamplifier headstages (Axona) were used to reduce cable movement artifacts. The electrophysiological signal was amplified, filtered (×1,000, bandpass filter 1–10,000 Hz, MCP Plus signal conditioner, Alpha Omega), digitized at 20 kHz (PCI-6259, National Instruments) and saved on a computer (http://savannah.nongnu.org/projects/kacq). Three light-emitting diodes of different colors were attached to the headstage to track the position of the animal during exploration. The video signal from a camera mounted on the ceiling was analyzed using a position tracking system, which saved the position of the light-emitting diodes at 25 Hz. The resolution of the camera was 5.8 pixels/cm. Spikes were extracted from the digitally bandpass filtered (0.8–5 kHz) signal, and their features were obtained using principal-component analysis. Spikes were separated into putative individual neurons via automatic clustering software (http://klustakwik.sourceforge.net/), before being manually refined using a graphical cluster cutting program. Only clusters that were stable for the duration of the recording session and with a clear refractory period (>1.5 ms) in their autocorrelation were analyzed further.

**Behavioral experiments.** After a 1 week recovery period, mice were maintained at 85–90% of their free-feeding weight and trained to forage in two different environments: an open field (70 cm × 70 cm × 30 cm high) and a zigzag maze with five alleys[42]. For familiarization to the open field, mice received 2–3 daily trials of 10 min during which 5 mg food pellets (AIN-76A Rodent Tablet, TestDiet) were delivered every 20–40 s. This was repeated for 7 d. On subsequent days, mice were connected to the recording system before being placed in the open field for training. Training continued until the mice explored readily in the entire open field. For familiarization with the zigzag maze, a mouse was first placed in the maze with food available at random locations for two 10 min daily sessions. On subsequent days, the food rewards were moved progressively until they were only available at the two ends of the maze. The mouse had to run from one end to the other to obtain food rewards. Mice were trained until they ran from one end to the other without much hesitation.

A recording session consisted of a series of nine 20-min trials, starting with a rest trial and then alternating between exploratory and rest trials. The open field and zigzag maze were used for the exploratory trials, following an ABAB protocol, where A and B indicate the two different environments. During the rest trials, mice were placed in a gray rest box (23 cm × 25 cm × 30 cm high).

**Laser stimulation.** During the recording session, the implanted optic fiber (multimode IRVIS fiber, numerical aperture (NA) = 0.22) was connected to a diode-pumped solid-state 473-nm laser (maximum, 25 mW; CrystaLaser). Laser pulses of 10 ms were delivered at a mean frequency of 6.67 Hz during the last trial of the recording session. Laser output power for the short pulse was 9.4 mW. Considering a model based on empirical measurements from mammalian brain tissue, a radiant flux of ~378 mW/mm$^2$ and 31 mW/mm$^2$ at 0.1 mm and 0.5 mm from the fiber tip can be predicted (http://www.stanford.edu/group/dlab/cgi-bin/graph/chart.php). In addition, laser stimulation (40 ms or 65 ms, 6.3 mW output power) was delivered at either the trough or the peak of theta oscillation during two of the four exploratory trials (abAB or ABab, where small letters represent trials with laser stimulation). The presence and phase of theta oscillations were detected online using a C program running on a computer equipped with a real-time Linux kernel (https://rt.wiki.kernel.org/). The last 500 ms of brain signal were bandpass-filtered at theta (6–10 Hz) and delta (2–4 Hz) frequencies. The power (root mean square) at theta and delta frequency was calculated. Theta oscillations were considered to be present if the theta/delta power ratio was larger than 1.75. Laser stimulation occurred if the calculated theta phase was within 10° from the stimulation phase.

**Identification of PV$^+$ interneurons.** PV$^+$ interneurons were identified based on their firing rate response to 10 ms laser pulses at a mean frequency of 6.67 Hz for 20 min. This pattern of stimulation allowed reliable activation of PV$^+$ interneurons and sufficient data to evaluate their firing behavior. The mean firing rate of each cell before and after the onset of the pulse was calculated in 1-ms time bins. The 50 ms preceding laser onset were used as baseline where the mean and s.d. of the firing rate were calculated. If the firing rate of a cell in the first 4 bins after laser onset was higher than 6 s.d. above the mean and the cell fired at least 90 spikes during the laser stimulation of the trial, the cell was classified as a PV$^+$ interneuron.

The mean waveform of neurons was calculated from the bandpass-filtered (0.5–5 kHz) signal. For each cell, the tetrode wire on which the amplitude of the spikes was largest was used. The trough-to-peak latency and peak asymmetry (ratio of the difference between right and left baseline-to-peak amplitudes and their sum)[43] were calculated in a 3-ms time window centered on the trough of the spikes.

**Classification of functionally defined cell types.** Cells in the MEC were assigned to one of ten functionally defined cell groups based on five parameters: spatial sparsity score, grid score, border score, head direction score and mean firing rate (**Table 1**). Spatial sparsity, grid scores and border scores were calculated from their firing-rate maps in the open field. These maps were constructed by dividing the recording environment into 2 cm × 2 cm bins. For analysis during theta phase-specific stimulation, the recording environment was divided into 3 cm × 3 cm bins to account for the reduced amount of data available for construction of a spatial firing map. Periods in which the mouse was running faster than 3 cm/s were considered. The time spent in every bin was first calculated, and the resulting occupancy map was smoothed with a Gaussian kernel function with a kernel s.d. of 1.5 cm (2 cm for analysis of data obtained during theta phase-specific stimulation). The firing-rate map of each cell was calculated by dividing the number of spikes emitted in a given bin by the time spent there. The firing-rate

maps were smoothed with the Gaussian kernel function. The spatial sparsity score was adapted from ref. 44:

$$1 - \left( \frac{\left( \sum_{i=1}^{N} p_i \lambda_i \right)^2}{\sum_{i=1}^{N} p_i \lambda_i^2} \right)$$

where $N$ is the number of bins in the firing-rate map, $p_i$ is the occupancy probability of bin $i$ in the firing-rate map, $\lambda_i$ is the mean firing rate in bin $i$. The grid score was computed from the spatial autocorrelation matrices of the firing-rate maps[1,5]. Each bin of a spatial autocorrelation matrix represented a Pearson correlation coefficient between all possible pairs of bins in a firing-rate map with a given spatial lag. The spatial lag associated with a particular bin of the matrix was determined by the location of that bin relative to the matrix center. Pearson correlations at spatial lags for which less than 20 pairs of firing rates were available were not calculated. A peak in the autocorrelation matrix was defined as more than 10 adjacent bins with a correlation coefficient higher than a peak detection threshold that could be set to 0.1, 0.2 or 0.3. A circular region of the spatial autocorrelation matrix containing up to six peaks, but excluding the central peak, was defined. Pearson correlation coefficients were calculated between that circular region of the matrix and a rotated version of it (by 30°, 60°, 90°, 120° and 150°). The grid score was obtained with the following formula

$$\frac{r_{60} + r_{120}}{2} - \frac{r_{30} + r_{90} + r_{150}}{3}$$

The border score was adapted from previous work[6] and calculated using the formula

$$\frac{CM - DM}{CM + DM}$$

The bins of the firing-rate map for which the firing was above 20% of the maximum firing rate in the map were labeled as high firing rate bins. *CM* is the proportion of high firing rate bins that were located directly along one of the walls of the open field. For each high firing rate bin, the closest distance to a wall was found. *DM* was the mean closest distance of high firing rate bins, weighted by the firing rate in each bin. *DM* was also normalized to the largest closest distance possible in the firing-rate map so that *DM* varied from 0 to 1. The head direction score of each cell was quantified by computing the length of the mean vector for the distribution of firing rate across all head directions (10° per bin).

**Firing fields in the zigzag maze.** Firing-rate maps for trials on the zigzag maze were constructed using the same method as for the open-field trials (2-cm bins). Also, the two-dimensional position data were transformed into one dimension. This was done by finding the linear vectors that best represented the path of the mouse on the maze. Each alley was represented by one vector and the turning points by two shorter vectors. For each position sample, the point on these vectors that was closest to the two-dimensional position of the animal was found. The summation of the length of the vectors from one end of the zigzag maze until this point represented the current linear position of the mouse. The runs toward each end of the maze were treated separately. Linear firing-rate maps were calculated using the same procedure and parameters as for the two-dimensional firing-rate maps, with the exception that the data were unidimensional. A linear place field was defined as a portion of the maze containing a bin with a firing rate > 5 Hz and extending in both directions until the firing rate dropped below 20% of the bin with the highest firing rate. Different fields from the same cell were treated separately.

**Cross-correlation analysis.** Spike-time cross-correlations were calculated for all possible cell pairs in a recording session using 100 ms time window and 1 ms bins[30]. A baseline ranging from −50 ms to 0 ms was used to estimate the mean and s.d. in the cross-correlation. A bin with a *z*-score > 6 located between time 0 and 4 ms was considered indicating a significant peak at short latency (for other *z*-scores and latencies, see **Supplementary Fig. 9**).

**Theta detection.** Theta oscillation was detected on each tetrode. The signal was bandpass-filtered at delta (2–4 Hz) and theta (6–10 Hz) frequency by applying a fast Fourier transform and multiplying the output with a Butterworth filter function. The power of the filtered signal (root mean square) was calculated in 500 ms time windows. Theta epochs were defined as windows with a theta/delta power ration >1.5.

Within these epochs, the raw signal was filtered at 5–14 Hz, and the positive-to-negative zero-crossings were detected and assigned phase 0°. The onset of the laser pulse, ranging from 0° to 360°, was linearly interpolated between these points.

**Histological analysis.** After the electrophysiological experiments, mice were deeply anesthetized with ketamine and xylazine, and perfused intracardially with saline, followed by 4% paraformaldehyde. The brains were removed and stored in 4% paraformaldehyde for 24 h at 4 °C. The brains were sliced in 50-µm-thick sagittal sections. Three out of four sections were stained with cresyl violet. The final position of the tetrode tips and the optic fiber were established using light microscopy. The remaining sections were used to examine the expression of the ChR2-mCherry fusion protein in the MEC using fluorescence microscopy. *PV-Cre–ROSA26* mice were generated by crossing *PV-Cre* mice and *ROSA26* mice, and immunohistochemical staining for parvalbumin and β-galactosidase was performed. Mice were perfused as described, and 50-µm-thick sagittal sections were cut. After washing with phosphate buffered saline (PBS, pH 7.4) multiple times, free-floating sections were permeabilized and blocked for 2 h with PBS (pH 7.4) containing 5% BSA and 0.2% Triton X-100. The incubation of the sections with primary antibodies (mouse anti-parvalbumin (Sigma-Aldrich P3088)[45], 1:3,000, rabbit anti–β-galactosidase (ICN/Cappel, 55976)[46], 1:3,000) was performed for 48 h at 4 °C. For double-labeling experiments, slices were incubated simultaneously with the two primary antibodies. Sections were washed with PBS (pH 7.4) and incubated with the secondary antibody for 2 h (Alexa Fluor 488 goat anti-mouse (Invitrogen), 1:1,000, Cy3 goat anti-rabbit (Invitrogen), 1:1,000). Primary and secondary antibodies were diluted in PBS (pH 7.4). After repeated washing with PBS (pH 7.4), the sections were mounted on 0.1% gelatin-coated glass slides and covered with Mowiol 40–88.

**Statistical analysis.** Statistical tests were used as indicated and performed in R. If not otherwise indicated, two-sided Wilcoxon rank sum test (*W*) or two-sided Wilcoxon signed-rank test for paired data (*V*) were performed. Categorical data were analyzed with Pearson's chi-squared test. ANOVAs were performed when making multiple comparisons. Data distribution was assumed to be normal, but this was not formally tested. No statistical methods were used to predetermine sample sizes, but our sample sizes are similar to those reported in previous publications[42] and similar to those generally employed in the field[38]. Data collection and analysis were not performed blind to the conditions of the experiments. Data were collected randomized with respect to phase of stimulation (trough versus peak) and condition (stimulation versus sham).


41. Klugmann, M. *et al.* Aav-mediated hippocampal expression of short and long homer1 proteins differentially affect cognition and seizure activity in adult rats. *Mol. Cell. Neurosci.* **28**, 347–360 (2005).
42. Allen, K., Fuchs, E.C., Jaschonek, H., Bannerman, D.M. & Monyer, H. Gap junctions between interneurons are required for normal spatial coding in the hippocampus and short-term spatial memory. *J. Neurosci.* **31**, 6542–6552 (2011).
43. Sirota, A. *et al.* Entrainment of neocortical neurons and gamma oscillations by the hippocampal theta rhythm. *Neuron* **60**, 683–697 (2008).
44. Skaggs, W.E., McNaughton, B.L., Wilson, M.A. & Barnes, C.A. Theta phase precession in hippocampal neuronal populations and the compression of temporal sequences. *Hippocampus* **6**, 149–172 (1996).
45. Meyer, A.H., Katona, I., Blatow, M., Rozov, A. & Monyer, H. *In vivo* labeling of parvalbumin-positive interneurons and analysis of electrical coupling in identified neurons. *J. Neurosci.* **22**, 7055–7064 (2002).
46. Slezak, M. *et al.* Transgenic mice for conditional gene manipulation in astroglial cells. *Glia* **55**, 1565–1576 (2007).





doi:10.1038/nn.3696